

Multiple superionic states in helium–water compounds

Cong Liu^{1,5}, Hao Gao^{1,5}, Yong Wang¹, Richard J. Needs², Chris J. Pickard^{3,4}, Jian Sun^{3,4}, Hui-Tian Wang^{1*} and Dingyu Xing¹

Superionic states are phases of matter that can simultaneously exhibit some of the properties of a liquid and of a solid. For example, in superionic ice, hydrogen atoms can move freely while oxygen atoms are fixed in their sublattice. ‘Superionicity’ has attracted much attention in both fundamental science and applications. Helium is the most inert element in nature and it is generally considered to be unreactive. Here, we use ab initio calculations to show that He and H₂O can form stable compounds within a large pressure range that can exist even close to ambient pressure. Surprisingly, we find that they can form two previously unknown types of superionic state under high pressure and high temperature. In the first of these phases, the helium atoms exhibit liquid behaviour within a fixed ice-lattice framework. In the second phase, both helium and hydrogen atoms move in a liquid-like fashion within a fixed oxygen sublattice. As the He–O interaction is weaker than the H–O interaction, the helium atoms in these superionic states have larger diffusion coefficients and lower ‘melting’ temperatures than those of hydrogen, although helium is heavier than hydrogen. The insertion of helium atoms substantially decreases the pressure at which superionic states may be formed, compared to those in pure ice.

The pioneering work of Demontis et al.¹ and Cavazzoni et al.² led to studies of the ‘hot ice’ layer between the rocky core and gaseous atmosphere in Uranus and Neptune, and proposed a surprising new phase between the solid and the fluid. This is a ‘superionic’ state that is characterized by a fixed sublattice of oxygen or nitrogen atoms, while the hydrogen atoms diffuse almost freely through the sublattice. Since then, many theoretical and experimental studies have been devoted to investigating this important state of matter^{3–20}. For instance, experimental electrical conductivity measurements^{3,4} and Raman signals⁵ of water under compression indicate the existence of superionic states. The superionic water seems to be adjacent to the ordered ice VII and ice X, and significant ionic conductivity is found¹⁰. Very recently, Millot et al.^{19,20} investigated water ice under shock compression conditions and showed that ice melts near 5,000 K at 190 GPa, which is close to the conditions found in the interiors of planets, and may have connections to superionic states.

Theoretical simulations were used to investigate the phase diagram of superionic water under conditions that may be found in planetary interiors^{7,8}. Recent simulations suggested that the oxygen sublattice in superionic water experiences a complicated evolution under compression, with phases such as body-centred cubic, face-centred cubic, closed-packed, $P2_1/c$ and so on^{11,12}. To study these transformations, thermodynamic potentials and entropies for superionic water were calculated¹⁴. Phases of superionic water (VII' and VII'') were proposed^{15,18}, and superionic states in ammonia and ammonia–water mixtures have also been investigated^{9,13,16,17}. For instance, Bethkenhagen et al.^{13,16} studied equations of state of mixtures of water, ammonia and methane, and developed a new model of the interior structure of Uranus. Jiang et al.¹⁷ found an ionic phase in ammonia dihydrate, which transforms into a superionic phase under high temperature and pressure. Due to the chemical similarity

of hydrogen and lithium, the mechanism of hydrogen diffusion in the superionic state has been used to explore ionic conductivity in electrodes and electrolyte materials, especially in lithium-based battery materials^{21–23}. It seems that superionic states also have connections with the recently discovered copper-based thermoelectric materials^{24,25}.

Knowledge of the behaviour of helium at different temperatures and pressures is key to understanding the nature of celestial bodies, as it is the second most abundant element in the Universe after hydrogen and it is also present in large quantities in the atmospheres of giant planets such as Uranus and Neptune. Helium, as the most inert element in the periodic table, is generally considered to be unreactive due to its stable closed-shell electronic configuration with filled *s* valence orbitals. Pressure is often used to explore new states of matter. Even a material as inert as helium can react with some elements and compounds under high pressure. For instance, a mixture with other inert gases^{26,27}, such as nitrogen^{28,29}, reacts with sodium³⁰, iron³¹ or iron peroxide³², alkali oxides or sulfide compounds³³ and alkaline earth fluorides³⁴. The addition of helium can also reduce the pressure at which polymerization of nitrogen may occur³⁵. It has been reported that helium can react with water to form He(H₂O)₂ at very high pressures (297 GPa)³⁶. Teeratchanan and Hermann³⁷ recently found that helium can fill the voids in ice clathrates at very low pressures.

However, there is still a gap between the pressure of a few gigapascals and that of 300 GPa that has not been explored in the helium–water system, although this turns out to be the pressure range in which superionic states can emerge in ice. On the other hand, helium compounds are not easily formed and superionicity in helium-based structures has not so far been reported. Moreover, the diffusive motions of helium in these compounds are also unknown. Beyond the ‘hot ice’ layer in Uranus and Neptune, helium is gaseous,

¹National Laboratory of Solid State Microstructures, School of Physics and Collaborative Innovation Center of Advanced Microstructures, Nanjing University, Nanjing, China. ²Theory of Condensed Matter Group, Cavendish Laboratory, Cambridge, UK. ³Department of Materials Science & Metallurgy, University of Cambridge, Cambridge, UK. ⁴Advanced Institute for Materials Research, Tohoku University, Sendai, Japan. ⁵These authors contributed equally: Cong Liu, Hao Gao. *e-mail: jiansun@nju.edu.cn; htwang@nju.edu.cn

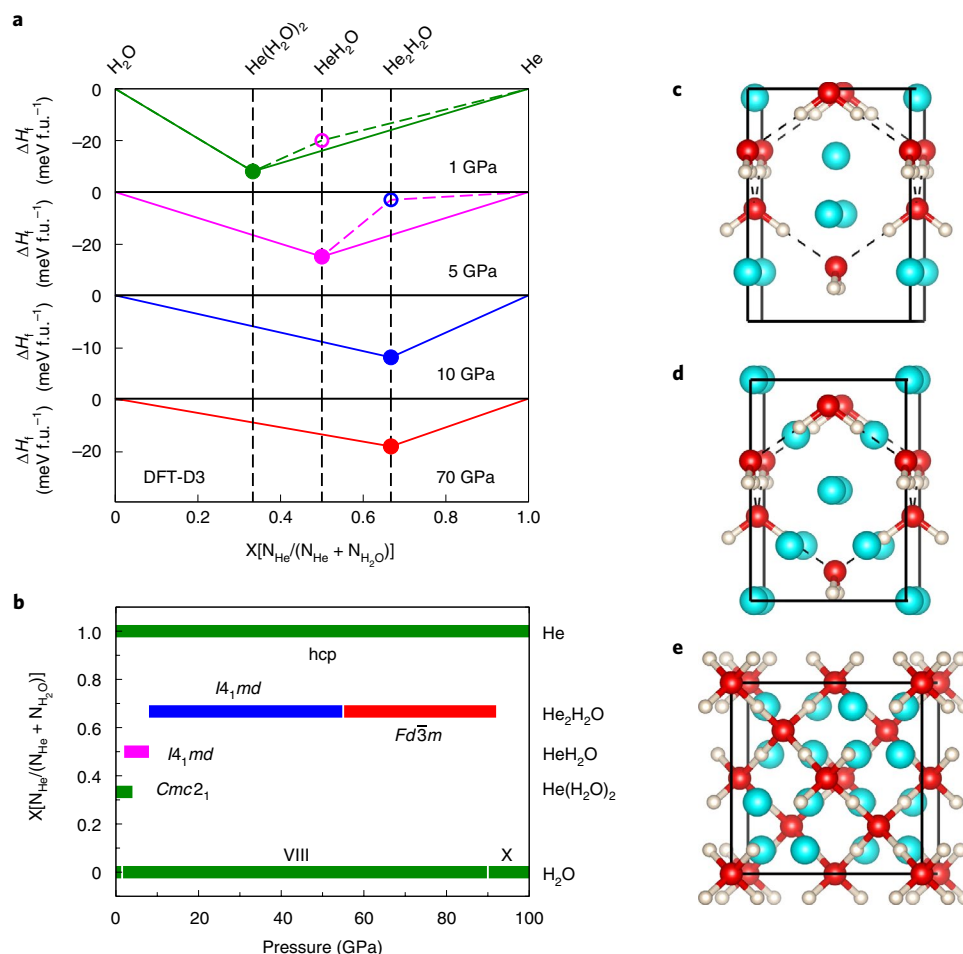


Fig. 1 | Thermodynamics of the He–H₂O system and crystal structures of the stable compounds. a, The convex hull for formation enthalpies (ΔH_f , with respect to He and H₂O) at different pressures, calculated with the DFT-D3 functional. **b**, The pressure–composition phase diagram of the He–H₂O phases (magenta, blue and red lines) discovered in this work, together with the previously known phases (green lines) below 100 GPa. **c–e**, The crystal structures of three representative new phases: *I*₄₁*md* HeH₂O (**c**), *I*₄₁*md* He₂H₂O (**d**) and *Fd* $\bar{3}$ *m* He₂H₂O (**e**).

which motivates exploration of the relationship between helium and water at low and medium pressures.

Results

Crystal structures. We have used first-principles crystal-structure searching techniques to determine the most stable phases of various compositions of He–H₂O. This has led us to predict two different stable stoichiometries, HeH₂O and He₂H₂O, which have lower formation enthalpies than mixtures of H₂O and He at 2–8 and 8–92 GPa, respectively, as shown in the convex hulls and the phase diagram of the pressure–composition in Fig. 1a,b. Some representative structures of these new phases adopt the tetragonal *I*₄₁*md* HeH₂O structure and the cubic *Fd* $\bar{3}$ *m* He₂H₂O structure, and the symmetry of the system changes from *I*₄₁*md* to *Fd* $\bar{3}$ *m* at around 55 GPa. At low pressures, the HeH₂O and He(H₂O)₂ compositions become energetically favourable. Our calculations suggest that the *I*₄₁*md* HeH₂O phase and the previously proposed clathrate structure *Cmc*2₁ phase He(H₂O)₂ (ref. 37) are stable even close to ambient pressure. We also note that van der Waals (vdW) effects play a dominant role in the stability of He–H₂O compounds under pressure, and the effect of volume reduction is also a key element, especially in He₂H₂O.

Our searches also provide other candidate structures that have enthalpies that are very close (less than 1 meV per atom) to the lowest enthalpy structures presented in the main text. For instance, the

energy of *P*4₃2₁ HeH₂O is very close to that of *I*₄₁*md* HeH₂O; the *Cmc*2₁ He₂H₂O structure has a similar enthalpy to that of *I*₄₁*md* He₂H₂O; while the enthalpy of a *P*6₃/*mmc* He₂H₂O phase is similar to that of *Fd* $\bar{3}$ *m* He₂H₂O. The relevant structures are listed in Supplementary Table 1. It is interesting that the ice framework of *P*6₃/*mmc* He₂H₂O is close to that of hexagonal ice, while the ice framework in *Fd* $\bar{3}$ *m* He₂H₂O appears similar to cubic ice.

As shown in Fig. 1d,e, the H₂O molecule sublattices in *I*₄₁*md* and *Fd* $\bar{3}$ *m* He₂H₂O are similar to those of ice VIII and ice X, respectively. As recently shown by Bronstein et al.³⁸, O–H–O bond symmetrization occurs at around 90–100 GPa when the protons are considered as classical particles, and 60–65 GPa for quantum protons. Therefore, the presence of helium significantly decreases the pressure at which hydrogen-bond symmetrization occurs in the helium–water system.

Diffusion of atoms. To study the dynamical properties of the predicted water–helium compounds, we have performed extensive ab initio molecular dynamics (AIMD) simulations within the pressure range 10–120 GPa and the temperature range 200–2,600 K. Diffusion coefficients were calculated for the oxygen, hydrogen and helium atoms from their mean-square displacements (MSDs). Superionic water is usually classified as one of three phases in terms of the diffusion coefficient of the H and O atoms: the solid phase ($D_{\text{O}} = 0$ and $D_{\text{H}} = 0$), the superionic (SI) phase ($D_{\text{O}} = 0$ and $D_{\text{H}} > 0$) and the fluid

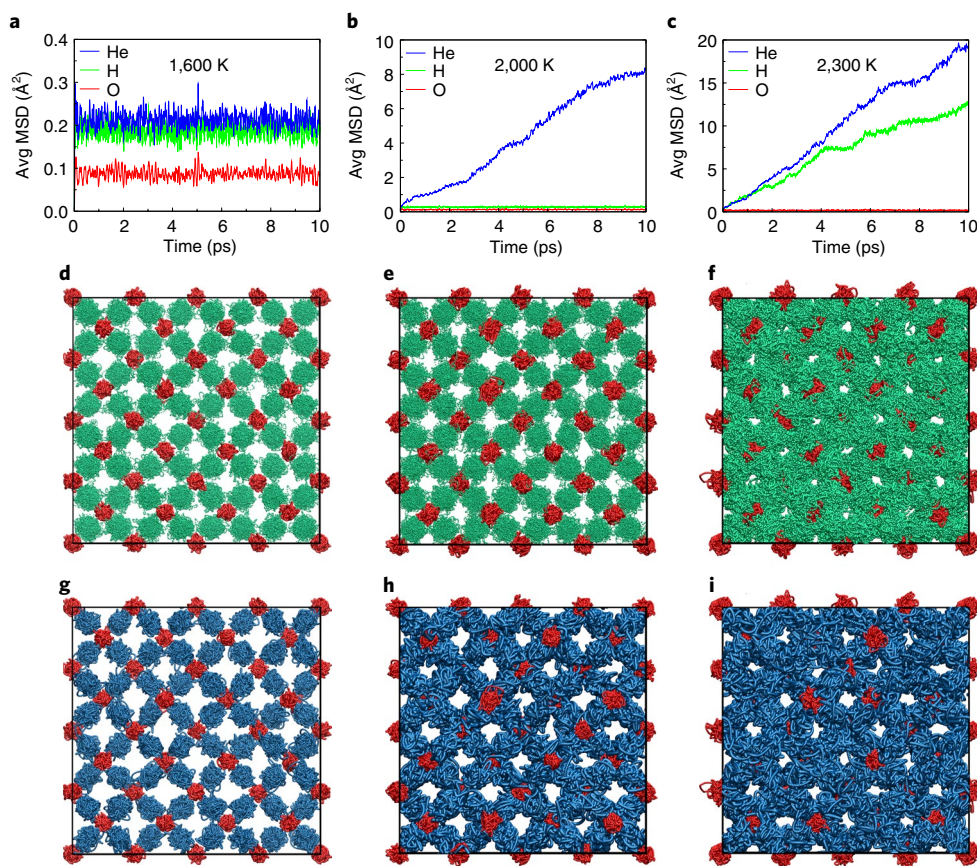


Fig. 2 | Behaviour of H and He atoms compared to O atoms in $Fd\bar{3}m$ $\text{He}_2\text{H}_2\text{O}$ from AIMD simulations at 1,600 K, 2,000 K and 2,300 K. a–c, The averaged MSDs for the H, He and O atoms from AIMD simulations at different temperatures. **d–i,** Representation of atomic trajectories in one supercell from the simulations from the last 5 ps run representing the three distinct phases: the solid phase (1,600 K), the superionic He phase (2,000 K), SI-I, and superionic He + H phase (2,300 K), SI-II. To avoid overlapping, only H and O are shown in **d–f**, and only He and O are shown in **g–i**.

phase ($D_{\text{O}} > 0$ and $D_{\text{H}} > 0$). Surprisingly, in our hydrated helium system, we found a region of superionicity with a new diffusive helium phase ($D_{\text{O}} = 0$, $D_{\text{H}} = 0$ and $D_{\text{He}} > 0$) that we have named as SI-I, and a coexisting diffusive helium and hydrogen phase ($D_{\text{O}} = 0$, $D_{\text{H}} > 0$ and $D_{\text{He}} > 0$) named SI-II, as shown in Fig. 2a–c. We have also confirmed our results from the radial distribution functions (RDFs) of the averaged structures, as shown in Supplementary Fig. 1. To confirm the superionic features we have distinguished the two superionic phases (SI-I and SI-II) by comparing their atomic trajectories from simulations at around 90 GPa, as shown in Fig. 2d–i.

The hydrogen and helium trajectories overlap with one another, and for clarity we show them in separate plots. Therefore, in Fig. 2d–f, only the oxygen and hydrogen atoms are plotted, while in Fig. 2g–i, only the oxygen and helium atoms are plotted. At around 90 GPa and a starting temperature below 1,600 K, the atoms are tethered at their starting positions and vibrate around them. From the diffusion constants of the atoms ($D_{\text{O}} = 0$, $D_{\text{H}} = 0$ and $D_{\text{He}} = 0$), one finds that helium hydride maintains the solid phase under these conditions.

However, when the temperature is increased to 2,000 K, although the oxygen and hydrogen atoms vibrate on their original sublattices, the helium atoms vibrate much more strongly and even jump to neighbouring sites, which results in a non-zero diffusion constant $D_{\text{He}} = 0.14 \times 10^{-8} \text{ m}^2 \text{ s}^{-1}$. At 2,300 K, both hydrogen and helium atoms are delocalized from their initial sites and their diffusion coefficients are both non-zero ($D_{\text{H}} = 0.21 \times 10^{-8} \text{ m}^2 \text{ s}^{-1}$ and $D_{\text{He}} = 0.33 \times 10^{-8} \text{ m}^2 \text{ s}^{-1}$). The diffusion coefficients calculated from the velocity autocorrelation functions are very similar to those

obtained from the MSD, as shown in Supplementary Table 2. Both helium and hydrogen atoms have larger diffusivities and therefore larger probabilities of moving into the interstitial spaces of the oxygen sublattice. Finally, increasing the temperature beyond 2,400 K leads to melting of the helium hydrate and all the atoms diffuse freely (not shown here).

Our simulations show that the three atomic species in helium hydrate (oxygen, hydrogen and helium) have different ‘melting’ temperatures above which diffusion occurs, $T_{\text{He}} < T_{\text{H}} < T_{\text{O}}$. The law of equipartition states that in equilibrium the energy should be equally distributed among the degrees of freedom. Therefore, with the same kinetic energy, the lighter atoms should move faster in non-interacting systems. Within our helium–water system, the helium atoms have a higher mobility and a lower ‘melting’ temperature than hydrogen atoms, although helium is heavier than hydrogen.

To investigate the reasons for this abnormal diffusive behaviour, we calculated the electron localization function of the hydrate $Fd\bar{3}m$ phase at 0 K, as shown in Supplementary Fig. 2. We plotted an electron localization function isosurface (isovalue = 0.7) in the conventional unit cell and a cross-section along the $\langle 011 \rangle$ plane. This demonstrates that electrons localize along the bonds between the oxygen and hydrogen atoms and are isolated in the helium atoms. This shows that the O–H interactions arise from strong covalent bonds while the helium atoms have weak vdW interactions with the H_2O framework. This results in a higher diffusion barrier for hydrogen atoms than for helium in the finite-temperature superionic phases.

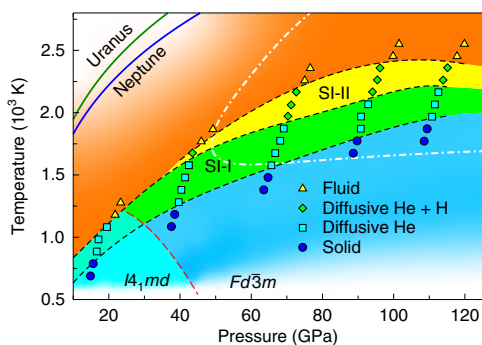


Fig. 3 | Proposed phase diagram of the helium–water system at high pressures obtained from our structure searches and AIMD simulations.

The symbols represent four distinct thermodynamic states sampled in our simulations: circle, solid state; square, He diffusive state (SI-I); diamond, both He and H diffusive state (SI-II); and triangle, fluid state. The black dashed lines were fitted to the phase boundaries. The red dashed line distinguishes the two predicted solid phases: $I4_1md$ and $Fd\bar{3}m$, as well as two types of H_2O sublattice ($I4_1md$ and $Fd\bar{3}m$) in the SI-I region. The isentropes for Uranus and Neptune (dark green and blue solid lines) and the phase boundary for superionic pure water (white dash-dotted line) are taken from ref. ⁸.

Phase diagram. Inspired by the temperature-induced features in helium hydrate discussed above, we expanded the pressure range studied to explore the superionic region from ambient pressure up to about 100 GPa with pressure steps of 20 GPa. In superionic water, the two different ‘melting’ temperatures of hydrogen and oxygen in ice divide its phase diagram into three regions: solid, superionic and liquid. As shown in Fig. 3, the three ‘melting’ temperatures of helium, hydrogen and oxygen divide the phase diagram of helium hydrate into four distinct regions: the solid, superionic helium (SI-I), superionic helium + hydrogen (SI-II) and fluid phases. As expected, the superionicity is enhanced with increasing pressure and the superionic helium region (SI-I) exists over the entire pressure range studied, while the superionic helium + hydrogen phase (SI-II) is stable only above 40 GPa. The pressure-induced transition from $I4_1md$ to $Fd\bar{3}m$ is in fact a continuous second-order phase transition, as shown in Supplementary Fig. 3. The temperature may therefore have a critical influence on the transition pressure between these two phases at high pressure.

Sun et al.¹² recently reported that the sublattice of the oxygen atoms in superionic water shows a complicated sequence of phase transitions. Examination of the trajectories in the superionic region obtained by averaging atomic positions shows that the oxygen sublattices in both SI-I and SI-II retain a face-centred cubic arrangement in helium hydrate, which has the same oxygen sublattices in solid $I4_1md$ and $Fd\bar{3}m$ He_2H_2O . Moreover, we have calculated RDFs for these averaged structures and compared them with the initial zero-temperature structure. At 30 GPa, the H_2O sublattice maintains its original positions as in the $I4_1md$ phase at low temperatures and then transforms into a sublattice of the $Fd\bar{3}m$ phase with increasing temperature, as shown in Supplementary Fig. 4.

Discussion

We have also studied superionicity in the low-pressure phase by gradually increasing the temperature in the AIMD simulations. The RDFs in Fig. 4 obtained from simulations at three different temperatures clearly indicate the presence of three states: the solid at 200 K, superionic helium at 500 K and a fluid phase at 800 K. HeH_2O maintains its crystalline form at 200 K, and almost all of the atomic pairs maintain their isolated peaks in the RDF, except the oxygen–helium

RDF, in which the combination of the first two peaks exhibits large thermal fluctuations.

In the superionic helium (SI-I) phase at 500 K, the thermal fluctuations increase rapidly and the peaks in the oxygen–oxygen, oxygen–hydrogen and hydrogen–hydrogen RDFs are slightly broadened, but they still show the characteristic peaks of a sublattice of H_2O undergoing large amplitude vibrations. The RDF involving helium atoms shows only one maximum and then converges to a constant intensity, which represents the behaviour of a liquid or a glass. Finally, at 800 K in the fluid phase, one can find from the hydrogen–hydrogen RDF that the H_2O sublattice is distorted. We find that the first peak still exists at the same position even in the fluid, and the O–H distance in the superionic state remains similar to that in ice.

Previous work¹⁴ shows that the quantum correction to the internal energy in molecular dynamics simulations is affected by the pressure and temperature in water ice. Our results (Supplementary Table 2) show that the nuclear quantum corrections u_{qc} for helium–water compounds are on a similar scale to those found in the literature for ice¹⁴. This is relatively small compared with the internal energy u_{md} , and therefore it does not greatly affect the occurrence of superionic phases in helium–water compounds.

In addition, Hermann et al.³⁹ studied zero-point energies (ZPEs) of water ice at megabar pressures by replacing hydrogen atoms with its isotopes, deuterium and tritium. The isotope effect can also emerge in the dynamical properties such as the diffusion coefficient and vibrational spectra. Here, we estimate the influence of nuclear quantum effects in the SI-I phase (at 2,000 K) and SI-II phase (at 2,400 K) by comparing the vibrational density of states (DOS) in He_2H_2O and He_2D_2O . As shown in Fig. 5, with increasing mass, in the zero-temperature phonon DOS, the high-frequency phonon peak decreases from about 3,000 cm^{-1} for hydrogen, to about 2,100 cm^{-1} for deuterium. At 2,000 K, both H and D are fixed in their sublattices and have very similar vibrational frequencies to their corresponding zero-temperature phonon frequencies. As shown in the insets, He atoms have a non-zero diffusive coefficient at zero frequency, which represents the SI-I phase. At 2,400 K, the H and D, as well as the He atoms have non-zero diffusive coefficients at zero frequency, while only the oxygen atoms are fixed, which corresponds to the SI-II phase. These results indicate that nuclear quantum effects do not significantly affect the existence of the superionic states in helium–water compounds.

In summary, we have used a combination of ab initio crystal structure searches and AIMD simulations based on density functional theory (DFT) to perform our calculations. We have systematically explored the helium–water phase diagram below 100 GPa and found three thermodynamically stable solid phases: the tetragonal $I4_1md$ HeH_2O , the $I4_1md$ He_2H_2O and the cubic $Fd\bar{3}m$ He_2H_2O phases. The pressure at which hydrogen-bond symmetrization occurs is reduced to around 55 GPa by introducing helium. More interestingly, we find a superionic helium region in the helium hydrate phase diagram with highly mobile helium atoms and a fixed sublattice of ice at relatively low temperatures. Further heating leads to a superionic phase in which the motions of hydrogen and helium atoms give rise to superionicity, while the oxygen atoms vibrate around the original sublattice. These three atomic types in the helium hydrate exhibit abnormal ‘melting’ properties ($T_{He} < T_H < T_O$) marked by a change in diffusion rates, molecular dynamics trajectories and RDFs. These properties divide the phase diagram into four distinguishable regions: solid, superionic helium, superionic helium + hydrogen and fluid. At relatively low pressures (below 40 GPa), the superionic helium + hydrogen region is absent and the superionic helium region remains close to ambient pressure. The insertion of helium substantially reduces the pressures at which superionic states can be formed compared to pure ice, which may be more easily accessed in future experiments. Although the

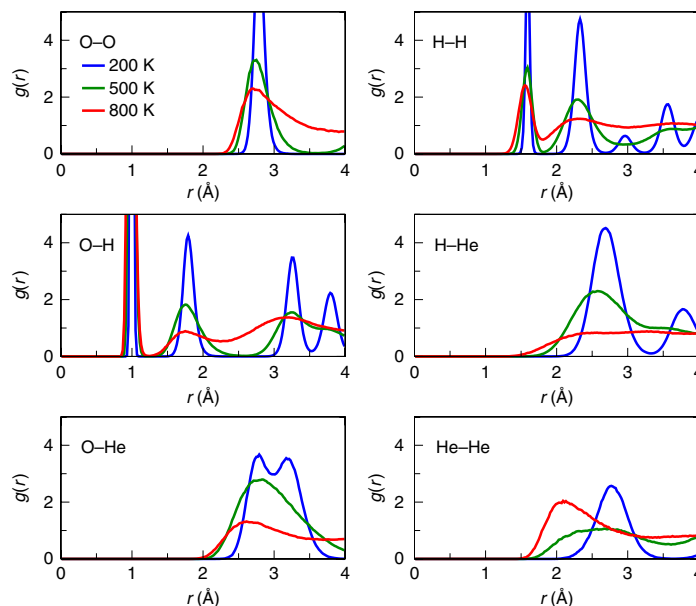


Fig. 4 | RDFs $g(r)$ of the $14,md$ HeH_2O phase. The AIMD simulations are performed at around 3 GPa and heating to around 200 K (blue lines), 500 K (green lines) and 800 K (red lines), corresponding to the solid phase, diffusive helium phase (SI-I) and fluid phase, respectively.

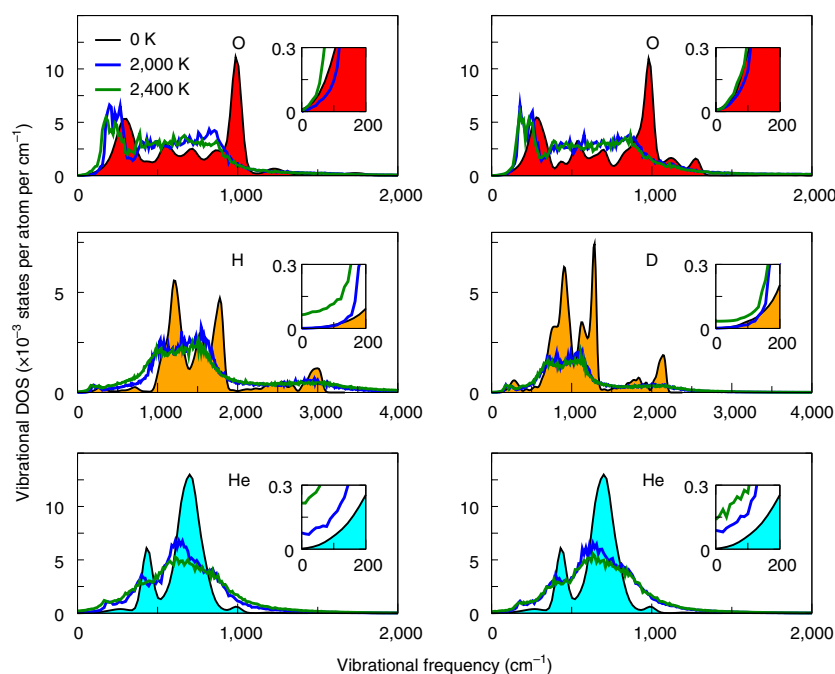


Fig. 5 | Vibrational DOS of $Fd\bar{3}m$ phase $\text{He}_2\text{H}_2\text{O}$ and $\text{He}_2\text{D}_2\text{O}$. The vibrational DOS for $\text{He}_2\text{H}_2\text{O}$ is shown on the left and that for $\text{He}_2\text{D}_2\text{O}$ is shown on the right. The coloured areas under the black curves give the phonon DOS of O (red), H/D (orange) and He (cyan) from static phonon calculations at 0 K. The blue and dark green lines represent the vibrational DOS of each atomic species in the SI-I phase at 2,000 K and the SI-II phase at 2,400 K, respectively, calculated from the Fourier transform of the velocity autocorrelation function. The low-frequency regions are enlarged in the insets and the zero/non-zero vibrational DOS at zero frequency shows the fixed/diffusive behaviour of O, H/D and He at different temperatures.

pressures and temperatures in this work are lower than those in the isentropes of Uranus or Neptune, the insertion of helium could alter the superionicity of pure water, which may still exist in Uranus or Neptune. Meanwhile, as the second most abundant element, helium may exist in planets or moons with different masses, compositions and distances from their own main stars. These planets and moons may have different isentropic conditions that could allow the formation of superionic $\text{He-H}_2\text{O}$ compounds.

Online content

Any methods, additional references, Nature Research reporting summaries, source data, statements of code and data availability and associated accession codes are available at <https://doi.org/10.1038/s41567-019-0568-7>.

Received: 22 October 2018; Accepted: 23 May 2019;
Published online: 1 July 2019

References

- Demontis, P., LeSar, R. & Klein, M. L. New high-pressure phases of ice. *Phys. Rev. Lett.* **60**, 2284–2287 (1988).
- Cavazzoni, C. et al. Superionic and metallic states of water and ammonia at giant planet conditions. *Science* **283**, 44–46 (1999).
- Yakushev, V., Postnov, V., Fortov, V. & Yakysheva, T. Electrical conductivity of water during quasi-isentropic compression to 130 GPa. *J. Exp. Theor. Phys.* **90**, 617–622 (2000).
- Chau, R., Mitchell, A., Minich, R. & Nellis, W. Electrical conductivity of water compressed dynamically to pressures of 70–180 GPa (0.7–1.8 Mbar). *J. Chem. Phys.* **114**, 1361–1365 (2001).
- Goncharov, A. F. et al. Dynamic ionization of water under extreme conditions. *Phys. Rev. Lett.* **94**, 125508 (2005).
- Goldman, N., Fried, L. E., Kuo, I.-F. W. & Mundy, C. J. Bonding in the superionic phase of water. *Phys. Rev. Lett.* **94**, 217801 (2005).
- French, M., Mattsson, T. R., Nettelmann, N. & Redmer, R. Equation of state and phase diagram of water at ultrahigh pressures as in planetary interiors. *Phys. Rev. B* **79**, 054107 (2009).
- Redmer, R., Mattsson, T. R., Nettelmann, N. & French, M. The phase diagram of water and the magnetic fields of Uranus and Neptune. *Icarus* **211**, 798–803 (2011).
- Ninet, S., Datchi, F. & Saitta, A. M. Proton disorder and superionicity in hot dense ammonia ice. *Phys. Rev. Lett.* **108**, 165702 (2012).
- Sugimura, E. et al. Experimental evidence of superionic conduction in H₂O ice. *J. Chem. Phys.* **137**, 194505 (2012).
- Wilson, H. F., Wong, M. L. & Militzer, B. Superionic to superionic phase change in water: consequences for the interiors of Uranus and Neptune. *Phys. Rev. Lett.* **110**, 151102 (2013).
- Sun, J., Clark, B. K., Torquato, S. & Car, R. The phase diagram of high-pressure superionic ice. *Nat. Commun.* **6**, 8156 (2015).
- Bethkenhagen, M., Cebulla, D., Redmer, R. & Hamel, S. Superionic phases of the 1:1 water–ammonia mixture. *J. Phys. Chem. A* **119**, 10582–10588 (2015).
- French, M., Desjarlais, M. P. & Redmer, R. Ab initio calculation of thermodynamic potentials and entropies for superionic water. *Phys. Rev. E* **93**, 022140 (2016).
- Hernandez, J.-A. & Caracas, R. Superionic phase transitions in body-centered cubic H₂O ice. *Phys. Rev. Lett.* **117**, 135503 (2016).
- Bethkenhagen, M. et al. Planetary ices and the linear mixing approximation. *Astrophys. J.* **848**, 67 (2017).
- Jiang, X., Wu, X., Zheng, Z., Huang, Y. & Zhao, J. Ionic and superionic phases in ammonia dihydrate NH₃·H₂O under high pressure. *Phys. Rev. B* **95**, 144104 (2016).
- Hernandez, J.-A. & Caracas, R. Proton dynamics and the phase diagram of dense water ice. *J. Chem. Phys.* **148**, 214501 (2018).
- Millot, M. et al. Experimental evidence for superionic water ice using shock compression. *Nat. Phys.* **14**, 297–302 (2018).
- Millot, M. et al. Nanosecond X-ray diffraction of shock-compressed superionic water ice. *Nature* **569**, 251–255 (2019).
- Kamaya, N. et al. A lithium superionic conductor. *Nat. Mater.* **10**, 682–686 (2011).
- Wang, X., Xiao, R., Li, H. & Chen, L. Oxsulfide LiAlSO: a lithium superionic conductor from first principles. *Phys. Rev. Lett.* **118**, 195901 (2017).
- He, X., Zhu, Y. & Mo, Y. Origin of fast ion diffusion in super-ionic conductors. *Nat. Commun.* **8**, 15893 (2017).
- Liu, H. et al. Copper ion liquid-like thermoelectrics. *Nat. Mater.* **11**, 422 (2012).
- Qiu, W. et al. Part-crystalline part-liquid state and rattling-like thermal damping in materials with chemical-bond hierarchy. *Proc. Natl Acad. Sci. USA* **111**, 15031–15035 (2014).
- Cazorla, C., Errandonea, D. & Sola, E. High-pressure phases, vibrational properties, and electronic structure of NeHe₂ and ArHe₂: a first-principles study. *Phys. Rev. B* **80**, 064105 (2009).
- Wang, Y., Zhang, J., Liu, H. & Yang, G. Prediction of the Xe–He binary phase diagram at high pressures. *Chem. Phys. Lett.* **640**, 115–118 (2015).
- Vos, W. L. et al. A high-pressure van der Waals compound in solid nitrogen–helium mixtures. *Nature* **358**, 46 (1992).
- Ninet, S., Weck, G., Loubeyre, P. & Datchi, F. Structural and vibrational properties of the van der Waals compound (N₂)₁₁He up to 135 GPa. *Phys. Rev. B* **83**, 134107 (2011).
- Dong, X. et al. A stable compound of helium and sodium at high pressure. *Nat. Chem.* **9**, 440–445 (2017).
- Monserat, B., Martinez-Canales, M., Needs, R. J. & Pickard, C. J. Helium–iron compounds at terapascal pressures. *Phys. Rev. Lett.* **121**, 015301 (2018).
- Zhang, J. et al. Rare helium-bearing compound FeO₂He stabilized at deep-earth conditions. *Phys. Rev. Lett.* **121**, 255703 (2018).
- Gao, H., Sun, J., Pickard, C. J. & Needs, R. J. Prediction of pressure-induced stabilization of noble-gas-atom compounds with alkali oxides and alkali sulfides. *Phys. Rev. Mater.* **3**, 015002 (2019).
- Liu, Z. et al. Reactivity of He with ionic compounds under high pressure. *Nat. Commun.* **9**, 951 (2018).
- Li, Y. et al. Route to high-energy density polymeric nitrogen t-N via He–N compounds. *Nat. Commun.* **9**, 722 (2018).
- Liu, H., Yao, Y. & Klug, D. D. Stable structures of He and H₂O at high pressure. *Phys. Rev. B* **91**, 014102 (2015).
- Teeratchanan, P. & Hermann, A. Computational phase diagrams of noble gas hydrates under pressure. *J. Chem. Phys.* **143**, 154507 (2015).
- Bronstein, Y., Depondt, P., Finocchi, F. & Saitta, A. M. Quantum-driven phase transition in ice described via an efficient Langevin approach. *Phys. Rev. B* **89**, 214101 (2014).
- Hermann, A., Ashcroft, N. W. & Hoffmann, R. Isotopic differentiation and sublattice melting in dense dynamic ice. *Phys. Rev. B* **88**, 214113 (2013).

Acknowledgements

J.S. gratefully acknowledges financial support from the MOST of China (grant nos. 2016YFA0300404 and 2015CB921202), the National Natural Science Foundation of China (grant nos. 11574133 and 11834006), the NSF of Jiangsu Province (grant no. BK20150012), the Science Challenge Project (no. TZ2016001), and the Fundamental Research Funds for the Central Universities and Special Program for Applied Research on Super Computation of the NSFC–Guangdong Joint Fund (the 2nd phase) under grant no. U1501501. C.J.P. and R.J.N. acknowledge financial support from the Engineering and Physical Sciences Research Council (EPSRC) of the UK under grants [EP/G007489/2] (C.J.P.) and [EP/P034616/1] (R.J.N.). C.J.P. also acknowledges financial support from the EPSRC and the Royal Society through a Royal Society Wolfson Research Merit award. The calculations were carried out using supercomputers at the High Performance Computing Center of Collaborative Innovation Center of Advanced Microstructures, the high-performance supercomputing centre of Nanjing University, ‘Tianhe-2’ at NSCC–Guangzhou and the CSD3 Peta4 CPU/KNL machine at the University of Cambridge.

Author contributions

J.S. conceived the project. J.S. and H.-T.W. led the project. C.L., H.G., Y.W. and C.J.P. performed the calculations. C.L., H.G., C.J.P. and J.S. analysed the data. C.L., J.S., R.J.N., H.-T.W. and D.X. wrote the manuscript. All authors discussed the results and commented on the manuscript.

Competing interests

C.J.P. is an author of the CASTEP code, and receives royalty payments from its commercial sales by Dassault Systèmes.

Additional information

Supplementary information is available for this paper at <https://doi.org/10.1038/s41567-019-0568-7>.

Reprints and permissions information is available at www.nature.com/reprints.

Correspondence and requests for materials should be addressed to J.S. or H.-T.W.

Peer review information: *Nature Physics* thanks Marius Millot and Ronald Redmer for their contribution to the peer review of this work.

Publisher's note: Springer Nature remains neutral with regard to jurisdictional claims in published maps and institutional affiliations.

© The Author(s), under exclusive licence to Springer Nature Limited 2019

Methods

We performed variable-composition structure predictions implemented in a machine-learning accelerated crystal structure search method⁴⁰. The crystal structures obtained were cross-checked with results from the ab initio random structure searching approach^{41,42}, which gave very similar results. The DFT calculations were performed using the Vienna ab initio simulation package⁴³. The projector augmented-wave method was used together with the generalized gradient approximation and the Perdew–Burke–Ernzerhof exchange correlation functional⁴⁴. We employed a plane-wave cutoff energy of 720 eV and a dense Monkhorst–Pack Brillouin zone integration grid with a resolution of $2\pi \times 0.025 \text{ \AA}^{-1}$. The relaxed ionic positions and cell parameters provided energy and forces that are smaller than 10^{-5} eV and $0.002 \text{ eV \AA}^{-1}$, respectively. The CASTEP code was used for the ab initio random structure searching approach searches; similar convergence parameters as used in the Vienna ab initio simulation package were employed⁴⁵. To account for the vdW interactions, we used the DFT-D3⁴⁶, optB88-vdW⁴⁷ and rev-vdW-DF2⁴⁸ functionals to cross-check the quality of the enthalpy calculations and the calculated ZPE. The results obtained with different functionals are very similar (see Supplementary Fig. 5). Phonon calculations show that the newly predicted structures are dynamically stable, as can be seen in Supplementary Fig. 6. Phonon spectra of the $I4_1md$ HeH₂O phases at 0 GPa do not exhibit imaginary vibrational frequencies, which indicates that it may be quenchable even to ambient pressure. Results for the ZPE, finite-temperature Gibbs free energy, and tests of the dynamical stability of the He–H₂O compounds are available in Supplementary Figs. 7 and 8. Phonon calculations were performed using the phonopy package⁴⁹. AIMD simulations were performed in $4 \times 4 \times 4$ supercells (with 256 atoms for HeH₂O and 320 atoms for He₂H₂O, respectively) with Γ -centred k -point sampling. The results of convergence tests for the k -point mesh and the finite-size effects are shown in Table 3 of the Supplementary Information. A Nose–Hoover thermostat was used to perform the NVT simulations. Runs with 7,000 steps were carried out with a time step of 1 fs, the initial 2 ps were used for thermalization and the final 5,000 steps of each trajectory

were used to extract the statistical quantities. Some trajectories were extended to 12 ps to check the stability of the simulations.

Data availability

The data that support the plots within this paper and other findings of this study are available from the corresponding authors upon reasonable request.

References

- Xia, K. et al. A novel superhard tungsten nitride predicted by machine-learning accelerated crystal structure search. *Sci. Bull.* **63**, 817–824 (2018).
- Pickard, C. J. & Needs, R. J. High-pressure phases of silane. *Phys. Rev. Lett.* **97**, 045504 (2006).
- Pickard, C. J. & Needs, R. J. Ab initio random structure searching. *J. Phys. Condens. Matter* **23**, 053201 (2011).
- Kresse, G. & Furthmüller, J. Efficient iterative schemes for ab initio total-energy calculations using a plane-wave basis set. *Phys. Rev. B* **54**, 11169–11186 (1996).
- Perdew, J. P. et al. Atoms, molecules, solids, and surfaces: applications of the generalized gradient approximation for exchange and correlation. *Phys. Rev. B* **46**, 6671–6687 (1992).
- Clark, S. J. et al. First principles methods using CASTEP. *Z. Kristallogr. Cryst. Mater.* **220**, 567–570 (2009).
- Grimme, S., Antony, J., Ehrlich, S. & Krieg, H. A consistent and accurate ab initio parametrization of density functional dispersion correction (DFT-D) for the 94 elements H–Pu. *J. Chem. Phys.* **132**, 154104 (2010).
- Klimeš, J., Bowler, D. R. & Michaelides, A. Chemical accuracy for the van der Waals density functional. *J. Phys. Condens. Matter* **22**, 022201 (2009).
- Hamada, I. van der Waals density functional made accurate. *Phys. Rev. B* **89**, 121103 (2014).
- Togo, A. & Tanaka, I. First principles phonon calculations in materials science. *Scr. Mater.* **108**, 1–5 (2015).